

Enhanced information content for three-dimensional localization and tracking using the double-helix point spread function with variable-angle illumination epifluorescence microscopy

Cite as: Appl. Phys. Lett. **110**, 211107 (2017); <https://doi.org/10.1063/1.4984133>

Submitted: 18 October 2016 . Accepted: 08 May 2017 . Published Online: 24 May 2017

Dapeng Wang, Anurag Agrawal , Rafael Piestun, and Daniel K. Schwartz



View Online



Export Citation



CrossMark

ARTICLES YOU MAY BE INTERESTED IN

[Total internal reflection fluorescence based multiplane localization microscopy enables super-resolved volume imaging](#)

Applied Physics Letters **110**, 211102 (2017); <https://doi.org/10.1063/1.4983786>

[Three-dimensional localization precision of the double-helix point spread function versus astigmatism and biplane](#)

Applied Physics Letters **97**, 161103 (2010); <https://doi.org/10.1063/1.3499652>

[Three-dimensional localization with nanometer accuracy using a detector-limited double-helix point spread function system](#)

Applied Physics Letters **95**, 021103 (2009); <https://doi.org/10.1063/1.3158923>



Instruments for Advanced Science

Contact Hiden Analytical for further details:

W www.HidenAnalytical.com

E info@hiden.co.uk

[CLICK TO VIEW](#) our product catalogue

Gas Analysis

- dynamic measurement of reaction gas streams
- catalysis and thermal analysis
- molecular beam studies
- dissolved species probes
- fermentation, environmental and ecological studies

Surface Science

- UHV/TPO
- SIMS
- end point detection in ion beam etch
- elemental imaging - surface mapping

Plasma Diagnostics

- plasma source characterization
- etch and deposition process reaction kinetic studies
- analysis of neutral and radical species

Vacuum Analysis

- partial pressure measurement and control of process gases
- reactive sputter process control
- vacuum diagnostics
- vacuum coating process monitoring

Enhanced information content for three-dimensional localization and tracking using the double-helix point spread function with variable-angle illumination epifluorescence microscopy

Dapeng Wang,^{1,a)} Anurag Agrawal,^{2,a)} Rafael Piestun,³ and Daniel K. Schwartz^{1,b)}

¹Department of Chemical and Biological Engineering, University of Colorado Boulder, Boulder, Colorado 80309, USA

²Double Helix LLC, Boulder, Colorado 80303, USA

³Department of Electrical, Computer, and Energy Engineering, University of Colorado Boulder, Boulder, Colorado 80309, USA

(Received 18 October 2016; accepted 8 May 2017; published online 24 May 2017)

The signal-to-noise ratio (SNR) and three-dimensional localization precision of a double helix point spread function (DH-PSF) can be significantly improved by applying variable-angle illumination epifluorescence microscopy (VAI, also commonly known as “pseudo-TIRF” or “quasi-TIRF”). Here, we performed a quantitative analysis of the dependence of SNR and localization precision on the number of measured photons and the incident angle for static particles under both low (at a planar index-matched interface) and high (within a porous silica matrix) fluorescent background conditions. We found that under noisier imaging conditions, the SNR and localization precision obtained using VAI are up to fivefold and threefold greater, respectively, than those obtained using epi-illumination. Moreover, we demonstrate that the combination of DH-PSF and VAI can significantly improve the accuracy of the measured diffusion coefficient for mobile particles, even at a relatively large distance (50 μm) from the boundary of the optical cell. *Published by AIP Publishing.* [<http://dx.doi.org/10.1063/1.4984133>]

Three-dimensional (3D) super-resolution localization and tracking have been of increasing interest^{1,2} due to their unique abilities to characterize dynamic molecular behavior in heterogeneous environments. Various schemes have been developed to achieve 3D localization, e.g., z-stacks using confocal imaging,³ multifocal imaging,⁴ orbital scanning,⁵ astigmatism,^{6–8} total internal reflection fluorescence microscopy (TIRFM),⁹ feedback approaches,^{10–13} stimulated emission depletion microscopy,¹⁴ and double-helix point spread function (DH-PSF) modulation.^{15,16} Each of these has advantages and disadvantages with respect to temporal and spatial resolution, as well as the ability to track multiple molecules simultaneously. In particular, DH-PSF enables simultaneous and high-throughput tracking of multiple particles/molecules within a field of view with the extended depth and high temporal and nanoscale spatial resolution.^{17–20} In a typical DH-PSF modulation, a standard Airy disc PSF splits into two lobes that rotate around their midpoint along the axial dimension. Thus, an emitter can be localized in 3D by determining the center of the two lobes and the angle between them. However, engineering the PSF into two lobes spreads the intensity of the emitter at nominal focus over more sensor pixels, decreasing the signal-to-noise ratio (SNR) per pixel, which is vital to the localization precision of dim emitters.^{21,22}

In general, SNR can be improved by increasing the excitation (laser) intensity. However, in many cases, this simultaneously leads to increased background levels and rapid

photo-bleaching of fluorescent emitters. Recently, Yu *et al.* demonstrated that the light-sheet microscopy (LSM) technique can improve the SNR of DH-PSF, compared to epifluorescence, by reducing the out-of-focus background, resulting in an improvement of localization precision by a factor of ~ 2 .²⁰ While LSM is a powerful approach, it is highly specialized, requiring a complex and custom-built arrangement of the illumination and detection paths and cannot be easily applied to typical wide-field or total internal reflection fluorescence (TIRF) microscopes that are available in most chemical and biological laboratories. In contrast, variable-angle illumination epifluorescence microscopy (VAI), also referred to as pseudo-TIRF or quasi-TIRF, is a straightforward and flexible means to illuminate a wide variety of bulk samples, using an inclined excitation source with an angle of incidence smaller than the critical angle. The angle of incidence can be varied continuously, enhancing the flexibility of the imaging conditions. Importantly, VAI is broadly accessible since the experimental realizations of VAI and TIRF are identical. In the TIRF mode, the illumination beam is incident at an angle higher than the critical angle for total internal reflection, and fluorescence excitation is provided by an evanescent field, dramatically reducing background fluorescence but severely limiting the sample depth at which imaging can be performed. In VAI, however, a highly inclined beam (at an angle smaller than the critical angle) propagates into the sample in a tilted slice in order to decrease the out-of-focus fluorescence.^{23–25} The combination of VAI and DH-PSF has, in the past, achieved successful tracking of single mRNA molecules in bacteria.²⁶ However, various previous studies have suggested that the applicability of VAI is limited to regions of interest within a few

^{a)}D. Wang and A. Agrawal contributed equally to this work.

^{b)}Author to whom correspondence should be addressed: daniel.schwartz@colorado.edu

micrometers of the coverslip.^{24,27–29} Since this is often cited as a limitation of VAI, it is important to determine the ability of the technique to track particles far from the sample boundary^{30,31} and to determine how this ability, the SNR, and localization precision depend on imaging conditions and parameters (e.g., noise level and angle of incidence).

In this letter, we present a systematic and quantitative evaluation of the SNR and localization precision of fluorescent dye-doped particles using either VAI (as a function of the incident angle) or wide-field epi-illumination (EPI) modes (henceforth referred to as epi-illumination) at low excitation intensities in order to mimic the behavior of a dim emitter, under low-noise and high-noise conditions. Two conditions were examined in detail: (1) immobile particles at a refractive index-matched interface between 2,2'-thiodiethanol and a microscope slide and (2) immobile particles on the interior walls of a porous material (inverse opal) with relatively high background fluorescence. Moreover, we examined the SNR of diffusing particles in bulk liquid at distances as large as 50 μm above a microscope slide surface using both VAI and epi-illumination modalities. The sample preparation is given in detail in the [supplementary material](#).

The DH-PSF was created using a Double Helix SPINDLETM module (Double Helix LLC, Boulder) that was attached in the image train of a Nikon Ti-Eclipse total internal reflection fluorescence microscope, as shown in Figs. 1(a) and 1(b). The details of experiments are described in the [supplementary material](#). The two illumination modalities, i.e., epi-illumination and VAI, can be realized by tuning the laser incident angle [Fig. 1(c)]. A laser beam with a high incident

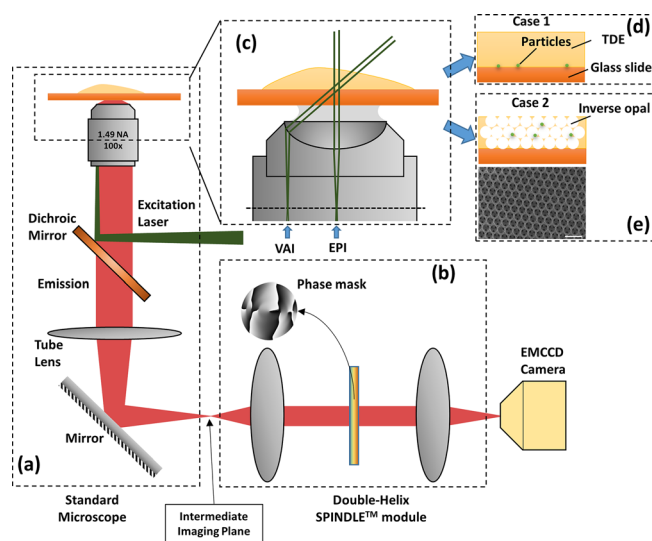


FIG. 1. Schematic of the experimental setup. (a) A standard Nikon Ti-Eclipse wide-field microscope. (b) The DH-PSF is implemented using a Double-Helix SPINDLETM module that resides between the microscope and the camera and relays the image plane through the Fourier domain where the phase mask is inserted to modulate the incoming light and engineer the PSF. (c) A magnified schematic of the two illumination modalities. In wide-field epi-illumination (EPI), the excited light enters along the optical axis, whereas in the VAI mode, the illumination enters near the edge of the objective and is capable of exciting a thin section (albeit thicker than that of total internal reflection illumination) of the specimen for better optical sectioning. Two cases were examined: (d) immobile fluorescent particles at a refractive index-matched interface and (e) particles adsorbed on the interior walls of an inverse opal with a high background. A top view scanning electron microscope image of an inverse opal is also shown.

angle, θ , illuminates the focal volume while minimizing the excitation of fluorophores/emitters in the out-of-focus volume,³² increasing the contrast of the fluorescence image significantly compared to that of images obtained using epi-illumination [Fig. 1(c)]. To demonstrate this quantitatively, we first obtained fluorescence images of particles at an index-matched thiodiethanol (TDE)/glass interface at varying θ [case 1 in Fig. 1(d)]. Even at a very low excitation intensity (0.06 mW), particles could be identified by discerning the two lobes of the DH-PSF at $\theta \geq 73^\circ$, indicating that VAI modulation effectively suppressed the background fluorescence to enhance SNR [Fig. 2(a)]. While particles could be observed using epi-illumination at a higher laser intensity (0.35 mW), the SNR was still much smaller than when using VAI modulation. To ensure that the SNR decrease was not caused by photo-bleaching of the fluorescent particles, the laser beam angle was varied from VAI to epi-illumination and back. Under these low power excitation conditions, the decrease in the number of photons detected due to bleaching was less than 3%–5%. Figures 2(c) and 2(d) demonstrate this

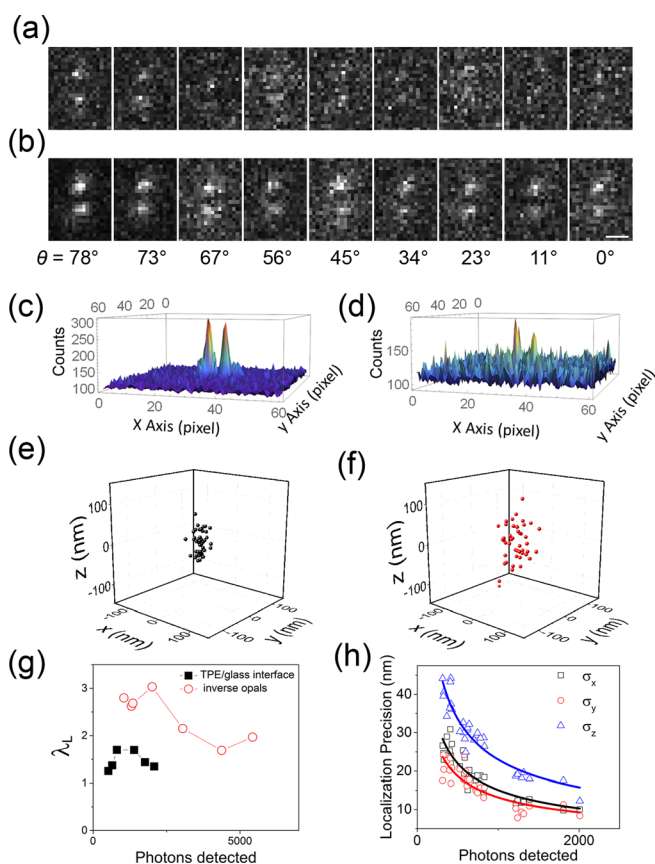


FIG. 2. DH-PSF images of a fluorescent bead excited at laser intensities of (a) 0.06 mW and (b) 0.35 mW, with the angle of the excitation beam, θ , ranging from 0° to 78° . The scale bar represents 1 μm . Heat-map representations of the fluorescence intensity of DH-PSF images of the same fluorescent particle excited by a laser intensity of 0.35 mW at (c) $\theta = 78^\circ$ or (d) 0° . Scatter plots of 50 3D localizations for a single fluorescent particle excited by a laser intensity of 0.35 mW at $\theta =$ (e) 78° or (f) 0° . (g) The improvement coefficient, λ_L (as defined in the text), as a function of the measured number of photons in the VAI mode for a particle adsorbed at a planar refractive index-matched interface (filled black squares) or within an inverse opal with high background fluorescence/scattering (open red circles). (h) The localization precision (standard deviation, σ) versus the number of photons (N) in the VAI mode. The data in all three dimensions are well-described by a power law function $\sigma_{x,y,z} \sim N^{-\alpha}$, where α is in the range of 0.5–0.55.

explicitly, showing heat-map representations of DH-PSF images of the same fluorescent particle at $\theta=78^\circ$ or 0° . Specifically, the number of photons detected above the background exhibited an approximately two-fold improvement in the VAI mode (see Table I, No. 4).

The 3D position of each emitter was determined using the DH-TRAXTM software (Double Helix LLC, Boulder) that fitted the two lobes of the DH-PSF using a double 2D Gaussian function.^{16,33} The lateral (x , y) particle position was determined by finding the midpoint of the two lobe centers, and the z position was extracted by interpolating the angle between two lobes from a calibration curve. The calibration curve was generated by recording images of a 100 nm fluorescent bead with ~ 6200 detected photons at different z positions operated by using a piezoelectric objective z -positioner with 100 nm increments over around $4 \mu\text{m}$. The number of photons was determined by summing the total intensity counts within the two lobes of the point spread function, subtracting the baseline camera bias (100 counts for the iXon) and multiplying the result by the ratio of pre-amplification/EM (electron multiplying) gain. The EM gain was controlled by the acquisition software, and the pre-amplification gain was obtained from the data sheet that was included with the camera.³⁴ To determine the localization precision of an immobile particle at a TDE/glass interface, we recorded 50 images at $\theta=0^\circ$ or 78° to measure the standard deviation of the 3D position. Representative examples obtained at an excitation intensity of 0.35 mW are shown in Figs. 2(e) and 2(f). The standard deviations of the measured mean positions in the x , y , and z dimensions represent the localization precisions σ_x , σ_y , and σ_z , respectively. The localization precision magnitude σ is defined as $\sigma = (\sigma_x^2 + \sigma_y^2 + \sigma_z^2)^{1/2}$.³⁵ Table I lists the localization precision and measured number of photons for a single fluorescent particle under VAI and epi-illumination excitation, clearly demonstrating that the localization precision was significantly improved in the VAI mode. To quantify the improvement in localization precision, we defined an improvement coefficient λ_L as the ratio of the localization precision magnitude in the VAI mode to that in epi-illumination, $\lambda_L = \sigma_{\text{VAI}}/\sigma_{\text{Epi}}$, for the same particle at the same laser intensity. Figure 2(g) shows λ_L as a function of the

number of photons detected in the VAI mode (filled black squares). Under these low background conditions, the improvement ratio was generally around $\lambda_L \approx 1.7$, indicating an approximate 50% improvement in localization precision.

Interestingly, the improvement in localization precision was even more dramatic under noisier imaging conditions, where fluorescent particles were immobilized inside an inverse opal. Again, the SNR and localization precision were obtained by acquiring 50 images at $\theta=0^\circ$ or 78° with laser intensities ranging from 0.15 to 1.18 mW. The results are listed in Table II, and Fig. 2(g) shows the improvement factor λ_L vs. photons measured above the background (open red circles). λ_L was as large as 3 at low intensities, decreasing to approximately 2 at strong excitation, indicating an improvement in the 200%–300% range. Moreover, we found that the SNR had an approximately fivefold increase (Table II), consistent with a previous observation of nuclear pore complexes on the nuclear envelope under high background conditions.²³ Taken together, these results indicated that the combination of VAI and DH-PSF is more effective when the background noise is high.

To better understand the reasons for improved localization precision using VAI, we plotted the localization precisions, σ_x , σ_y , and σ_z , for a particle with 300–2000 measured photons per frame as the incident angle θ was varied in the range of 0° – 78° using three different laser intensities (0.58 mW, 0.90 mW, and 1.18 mW). As shown in Fig. 2(h), the localization error decreases nonlinearly with an increase in the number of photons. The plot was well described by a power law function, $\sigma_{x,y,z} \sim N^{-\alpha}$, where α was in the range of 0.5–0.55 and N represents the number of photons. This explicitly demonstrates that the increase in localization precision is simply a function of the number of photons detected over background and follows a well-established relationship.^{21,36,37}

To assess the ability of the combination of VAI and DH-PSF in dynamic experiments for low photon count applications, we tracked 3D particle diffusion in the TDE solution at a vertical distance of $50 \mu\text{m}$ above the bottom glass surface of the liquid cell. The concentration was adjusted to ensure that fewer than 10 particles were observed in a $40 \times 40 \mu\text{m}$ view in each frame. Five movies with 3 min

TABLE I. Number of measured photons above the background and localization precision, σ , σ_x , σ_y , and σ_z , for a single particle immobilized at a TDE/glass interface imaged using VAI or epi-illumination at varying laser intensities.

Expt #	Laser intensity (mW)	Photons measured	σ_x (nm)	σ_y (nm)	σ_z (nm)	σ (nm)	Type of illumination
1	0.06	270 ± 69	27.8	22.2	42.4	55.3	VAI
		Epi
2	0.15	521 ± 89	18.4	15.6	22.9	33.3	VAI
		224 ± 52	34.5	33.3	37.5	41.6	Epi
3	0.26	653 ± 97	17.6	10.1	21.8	29.8	VAI
		334 ± 59	21.8	23.9	33.02	40.8	Epi
4	0.35	812 ± 121	15.5	10.1	17.3	25.3	VAI
		384 ± 73	25.5	17.1	30.1	43.0	Epi
5	0.58	1396 ± 180	12.4	8.2	12.0	19.1	VAI
		598 ± 99	17.4	16.5	21.8	32.4	Epi
6	0.90	1768 ± 162	7.6	7.1	16.4	19.4	VAI
		756 ± 100	14.2	13.2	20.1	27.9	Epi
7	1.18	2080 ± 209	9.4	6.7	9.9	15.2	VAI
		1012 ± 126	10.0	9.6	15.1	20.5	Epi

TABLE II. Number of photon and localization precision, σ_x , σ_y , σ_z , of a single particle immobilized on the interior walls of an inverse opal imaged using VAI or epi-illumination at varying laser intensities.

Expt #	Laser intensity (mW)	Photons measured	σ_x (nm)	σ_y (nm)	σ_z (nm)	σ (nm)	Type of illumination
1	0.15	1049 \pm 116	12.3	10.2	15.7	22.4	VAI
		210 \pm 54	28.4	27.0	49.0	62.7	Epi
2	0.2	6051 \pm 136	8.9	8.5	14.7	19.2	VAI
		1307 \pm 56	30.0	25.8	31.2	50.4	Epi
3	0.26	1356 \pm 157	10.2	8.2	12.7	18.2	VAI
		306 \pm 54	26.5	22.3	34.7	49.0	Epi
4	0.35	2012 \pm 138	7.1	5.9	11.2	14.6	VAI
		404 \pm 74	25.4	20.2	29.9	44.2	Epi
5	0.58	3051 \pm 218	6.5	4.7	9.4	12.4	VAI
		743 \pm 79	15.3	12.2	18.0	26.6	Epi
6	0.90	4376 \pm 364	6.1	4.8	15.1	17.0	VAI
		992 \pm 145	12.4	9.6	24.0	28.7	Epi
7	1.18	5428 \pm 522	5.0	3.8	9.4	11.3	VAI
		1223 \pm 151	12.8	8.6	15.8	22.1	Epi

duration were continuously captured at multiple lateral locations. The acquisition time for each frame was 0.05 s under laser excitation at 0.35 mW/cm². Adjacent identified positions were linked to establish trajectories using a custom-developed algorithm that was previously described.³¹ Each track was terminated when a particle diffused out of the field of view or focal volume or was photobleached. A typical trajectory is illustrated in Fig. 3(a). Notably, in a 15 min period, a total of 2594 and 503 trajectories (with lengths longer than 3 steps) were acquired using VAI and epi-illumination for the same solution, respectively. We found that the number of trajectories and the mean number of photons detected in two illumination modes were different [Figs. 3(b) and 3(c)]. Specifically, the mean photon count using VAI was approximately 1.4 times larger than that using epi-illumination. This value was consistent at imaging depths in the range of 10–50 μm above the bottom glass surface. In fact, this value vastly underestimates the actual improvement because relatively dimmer particles have much lower SNR in epi-illumination and were therefore not even detected by the localization algorithm.

We further quantified the ensemble-average mean squared displacement (MSD) according to $\langle r(\Delta t)^2 \rangle = \langle [r(t + \Delta t) - r(t)]^2 \rangle$, where $r(t)$ denotes the 3D position at time t , and the brackets represent the ensemble average. Figure 2(c) shows the ensemble-average MSD versus Δt . The plot of MSD versus Δt was well described by the relation $\langle r(\Delta t)^2 \rangle = 6D_{\text{bulk}}\Delta t$, to yield the average bulk diffusion coefficients $D_{\text{VAI}} = 0.22 \pm 0.01$ and $D_{\text{Epi}} = 0.17 \pm 0.01 \mu\text{m}^2/\text{s}$ when using VAI and

epi-illumination modes, respectively. Since the particle solution was identical in the two cases, we hypothesized that this difference was due to the fact that smaller and more weakly fluorescent particles were not identified in the epi-illumination mode, thereby biasing the observations to the brighter objects. To test this interpretation, we analyzed only the brighter trajectories obtained using VAI by removing trajectories with mean photon counts less than 500. Indeed, the MSD as a function of Δt from these filtered trajectories [open black squares in Fig. 3(c)] coincided with the data obtained by epi-illumination, yielding a diffusion coefficient of $0.17 \pm 0.01 \mu\text{m}^2/\text{s}$. These results demonstrate that insufficient SNR can cause biased diffusion results because of a potential correlation between fluorescent intensity and diffusion coefficient on a particle-by-particle basis.

Using the Stokes-Einstein equation, the measured diffusion coefficient ($0.22 \pm 0.01 \mu\text{m}^2/\text{s}$) corresponded to a hydrodynamic radius of ~ 15 nm, compared with the nominal radius of ~ 10 nm as quoted by the manufacturer. The hydrodynamic radius is often found to be larger than the physical particle size as determined using electron microscopy.^{38–40}

In summary, we have provided a quantitative analysis of how the combination of VAI and DH-PSF improves the SNR and 3D localization precision. The explicit connection between the localization precision and number of photons above the background under low and high noise conditions are listed in Tables I and II. We found that the improvements associated with VAI were more dramatic under noisier imaging conditions. In particular, the localization precision of a

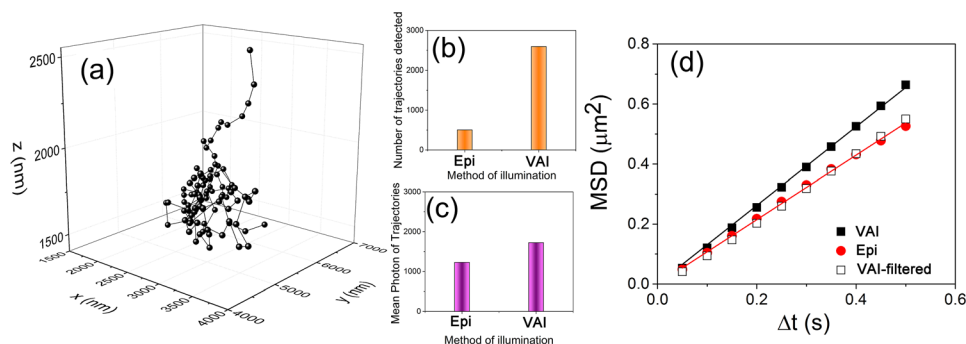


FIG. 3. (a) A representative trajectory with 95 steps taken by the VAI mode in the TDE solution. (b) Number and (c) mean photon counts of trajectories accumulated using VAI or epi-illumination under the same experimental conditions. (d) Ensemble MSD vs lag time for diffusing particles in the bulk solution imaged by both illumination modalities. The “VAI-filtered” data refer to the analysis of “brighter” particles as described in the main text. Solid lines indicate linear fits.

dim emitter was increased by a factor as large as 3 under conditions with high background fluorescence/scattering. We also demonstrated that the combination of DH-PSF and VAI can improve the accuracy of the measured diffusion coefficient for mobile particles, even at relatively large distances (50 μm) from the boundary of the optical cell. Finally, we would like to highlight that the use of VAI can be extended to other image-based 3D localization techniques, especially techniques involving PSF engineering.^{17,41–47}

See [supplementary material](#) for details of the sample preparation and the imaging setup.

This work was supported by the U.S. Department of Energy, Office of Science, Basic Energy Sciences, under Award No. #DE-SC0001854, by the National Science Foundation Small Business Innovation Research, under Award No. #IIP-1353638 (Double Helix LLC), and by NSF Award Nos. #1556473 and 1548924.

- ¹L. Mockl, D. C. Lamb, and C. Brauchle, *Angew. Chem., Int. Ed.* **53**, 13972 (2014).
- ²S. W. Hell, S. J. Sahl, M. Bates, X. Zhuang, R. Heintzmann, M. J. Booth, J. Bewersdorf, G. Shtengel, H. Hess, P. Tinnefeld, A. Honigmann, S. Jakobs, I. Testa, L. Cognet, B. Lounis, H. Ewers, S. J. Davis, C. Eggeling, D. Klennerman, K. I. Willig, G. Vicidomini, M. Castello, A. Diaspro, and T. Cordes, *J. Phys. D: Appl. Phys.* **48**, 443001 (2015).
- ³H. Bornfleth, P. Edelmann, D. Zink, T. Cremer, and C. Cremer, *Biophys. J.* **77**, 2871 (1999).
- ⁴S. Ram, P. Prabhat, J. Chao, E. S. Ward, and R. J. Ober, *Biophys. J.* **95**, 6025 (2008).
- ⁵Y. Katayama, O. Burkacky, M. Meyer, C. Braeuchle, E. Gratton, and D. C. Lamb, *ChemPhysChem* **10**, 2458 (2009).
- ⁶L. Holtzer, T. Meckel, and T. Schmidt, *Appl. Phys. Lett.* **90**, 053902 (2007).
- ⁷B. Huang, W. Q. Wang, M. Bates, and X. W. Zhuang, *Science* **319**, 810 (2008).
- ⁸J. Min, S. J. Holden, L. Carlini, M. Unser, S. Manley, and J. C. Ye, *Biomed. Opt. Express* **5**, 3935 (2014).
- ⁹K. D. Kihm, A. Banerjee, C. K. Choi, and T. Takagi, *Exp. Fluids* **37**, 811 (2004).
- ¹⁰M. F. Juetten and J. Bewersdorf, *Nano Lett.* **10**, 4657 (2010).
- ¹¹I. M. Peters, B. G. de Grooth, J. M. Schins, C. G. Figdor, and J. Greve, *Rev. Sci. Instrum.* **69**, 2762 (1998).
- ¹²G. A. Lessard, P. M. Goodwin, and J. H. Werner, *Appl. Phys. Lett.* **91**, 224106 (2007).
- ¹³A. Dupont and D. C. Lamb, *Nanoscale* **3**, 4532 (2011).
- ¹⁴B. Harke, C. K. Ullal, J. Keller, and S. W. Hell, *Nano Lett.* **8**, 1309 (2008).
- ¹⁵S. R. P. Pavani, M. A. Thompson, J. S. Biteen, S. J. Lord, N. Liu, R. J. Twieg, R. Piestun, and W. E. Moerner, *Proc. Natl. Acad. Sci. U.S.A.* **106**, 2995 (2009).
- ¹⁶S. R. P. Pavani and R. Piestun, *Opt. Express* **16**, 22048 (2008).
- ¹⁷G. Grover, S. R. P. Pavani, and R. Piestun, *Opt. Lett.* **35**, 3306 (2010).

- ¹⁸M. Badieirostami, M. D. Lew, M. A. Thompson, and W. E. Moerner, *Appl. Phys. Lett.* **97**, 161103 (2010).
- ¹⁹A. Gahlmann, J. L. Ptasin, G. Grover, S. Quirin, A. R. S. von Diezmann, M. K. Lee, M. P. Backlund, L. Shapiro, R. Piestun, and W. E. Moerner, *Nano Lett.* **13**, 987 (2013).
- ²⁰B. Yu, J. Yu, W. Li, B. Cao, H. Li, D. Chen, and H. Niu, *Appl. Opt.* **55**, 449 (2016).
- ²¹H. L. Lee, S. J. Sahl, M. D. Lew, and W. E. Moerner, *Appl. Phys. Lett.* **100**, 153701 (2012).
- ²²M. A. Thompson, M. D. Lew, M. Badieirostami, and W. E. Moerner, *Nano Lett.* **10**, 211 (2010).
- ²³M. Tokunaga, N. Imamoto, and K. Sakata-Sogawa, *Nat. Methods* **5**, 159 (2008).
- ²⁴C. A. Konopka and S. Y. Bednarek, *Plant J.* **53**, 186 (2008).
- ²⁵B. Cui, C. Wu, L. Chen, A. Ramirez, E. L. Bearer, W.-P. Li, W. C. Mobley, and S. Chu, *Proc. Natl. Acad. Sci. U.S.A.* **104**, 13666 (2007).
- ²⁶M. A. Thompson, J. M. Casolari, M. Badieirostami, P. O. Brown, and W. E. Moerner, *Proc. Natl. Acad. Sci. U.S.A.* **107**, 17864 (2010).
- ²⁷H. V. Mudrakola, K. Zhang, and B. Cui, *Structure* **17**(11), 1433 (2009).
- ²⁸K. Zhang, P. D. Chowdary, and B. Cui, *Rab GTPases: Methods Protocols* (Humana Press, 2015), p. 319.
- ²⁹W. Sun, A. Xu, K. Marchuk, G. Wang, and N. Fang, *J. Lab. Autom.* **16**(4), 255 (2011).
- ³⁰J. Vangindertael, I. Beets, S. Rocha, P. Dedeker, L. Schoofs, K. Vanhoorelbeeke, J. Hofkens, and H. Mizuno, *Sci. Rep.* **5**, 13532 (2015).
- ³¹D. P. Wang, C. L. He, M. P. Stoykovich, and D. K. Schwartz, *ACS Nano* **9**, 1656 (2015).
- ³²S. J. Lord, H. L. D. Lee, and W. E. Moerner, *Anal. Chem.* **82**, 2192 (2010).
- ³³A. Barsic, G. Grover, and R. Piestun, *Sci. Rep.* **4**, 5388 (2014).
- ³⁴See <http://www.andor.com/learning-academy/count-convert-quantifying-data-in-electrons-and-photons> for information about converting digital counts to detected photons.
- ³⁵H. Deschout, F. C. Zanacchi, M. Mlodzianoski, A. Diaspro, J. Bewersdorf, S. T. Hess, and K. Braeckmans, *Nat. Methods* **11**, 253 (2014).
- ³⁶R. E. Thompson, D. R. Larson, and W. W. Webb, *Biophys. J.* **82**, 2775 (2002).
- ³⁷E. Betzig, G. H. Patterson, R. Sougrat, O. W. Lindwasser, S. Olenych, J. S. Bonifacino, M. W. Davidson, J. Lippincott-Schwartz, and H. F. Hess, *Science* **313**, 1642 (2006).
- ³⁸B. Coldren, R. Van Zanten, M. J. Mackel, J. A. Zasadzinski, and H.-T. Jung, *Langmuir* **19**(14), 5632 (2003).
- ³⁹H. P. Erickson, *Biol. Proced. Online* **11**, 32 (2009).
- ⁴⁰M. J. Skaug, L. Wang, Y. Ding, and D. K. Schwartz, *ACS Nano* **9**(2), 2148 (2015).
- ⁴¹Y. Shechtman, S. J. Sahl, A. S. Backer, and W. E. Moerner, *Phys. Rev. Lett.* **113**, 133902 (2014).
- ⁴²S. Jia, J. C. Vaughan, and X. W. Zhuang, *Nat. Photonics* **8**, 302 (2014).
- ⁴³B. Shuang, W. Wang, H. Shen, L. J. Tauzin, C. Flatebo, J. Chen, N. A. Moringo, L. D. Bishop, K. F. Kelly, and C. F. Landes, *Sci. Rep.* **6**, 30826 (2016).
- ⁴⁴R. Piestun, C. J. Cogswell, A. D. Greengard, and Y. Y. Schechner, US Google patents (2010).
- ⁴⁵R. Piestun and S. A. Quirin, US Google patents (2013).
- ⁴⁶M. D. Lew, S. F. Lee, M. Badieirostami, and W. E. Moerner, *Opt. Lett.* **36**, 202 (2011).
- ⁴⁷S. J. Holden, T. Pengo, K. L. Meibom, C. F. Fernandez, J. Collier, and S. Manley, *Proc. Natl. Acad. Sci. U.S.A.* **111**(12), 4566 (2014).